*Journal of Applied Fluid Mechanics*, Vol. 15, No. 4, pp. 1017-1034, 2022.
Available online at www.jafmonline.net, ISSN 1735-3572, EISSN 1735-3645.
https://doi.org/10.47176/jafm.15.04.33209

# Free and Non-Free Vortex Design for Axial Fans with Circumferential Sweep through CFD Techniques

T. M. Arispe Angulo[1†], R. G. Ramirez Camacho[1], W. de Oliveira[1], E. R. da Silva[1], G. E. Niño Del Río[2]

[1] *Federal University of Itajubá, Itajubá, MG, 37500-903, Brazil*
[2] *ECCI University, Bogotá, Cundinamarca, 111311, Colombia*

†*Corresponding Author Email: tani.arispe@unifei.edu.br*

(Received July 17, 2021; accepted March 25, 2022)

## ABSTRACT

The sound generated by axial flow fans has become increasingly important in several industrial areas. These devices represent considerable noise sources that must be considered from the design stage. The scope of this research work is to present an axial fan design methodology based on the theory of the wing lift and to compare the aerodynamic and aeroacoustics behavior with the free vortex and the non-free vortex conditions. The effect of forward circumferential sweep on the rotor blades is analyzed in both conditions, which consists of a displacement in the tangential direction in the direction of rotor rotation. A cubic polynomial function is proposed for the construction of the blade geometry with circumferential sweep. It defines the center line of the blade and it is taken at 50% of the leading edge of each blade profile. The methodology for analyzing aeroacoustics behavior in fans is based on the integration of Computational Aeroacoustics and Computational Fluid Dynamics in order to analyze aerodynamic behavior, sound power level and sound pressure level at the preliminary design stage. It was verified that although both rotors present a similar aerodynamic behavior (the NFV rotor has a slightly lower performance), according to the analysis of local sound sources, the NFV rotor presents a slight decrease in the sound sources. It was also verified that the NFV rotor presents 2.2 dB less in sound pressure level than the FV rotor.

**Keywords**: CFD analysis; Design; Axial flow fan; Circumferential sweep; Aeroacoustics; Computational Fluid Dynamic; Free Vortex; Non-Free Vortex.

## NOMENCLATURE

| | |
|---|---|
| $b$ | blade span |
| $c$ | absolute flow velocity, constant |
| $C_D$ | drag coefficient |
| $C_L$ | lift coefficient |
| $d$ | constant |
| $D_e$ | rotor outer diameter |
| $D_i$ | rotor inner diameter |
| $e_{max}$ | maximum thickness |
| $F_B$ | force on the blade |
| $F_D$ | drag force |
| $F_L$ | lift force |
| $i$ | flow incidence angle |
| $l$ | length of chord |
| $n$ | axial fan rotor rotation |
| $N$ | number of axial rotor blades |
| $n_{qA}$ | specific rotation according to addison |
| $r$ | polar radius |
| $t$ | pitch |
| $u$ | circumferential velocity of the rotor |
| $\dot{V}$ | volumetric flow |
| $w$ | relative flow velocity |
| $w_\infty$ | mean velocity of relative flow |
| $x$ | radius ratio |
| $Y$ | fan specific work |
| $Y_B$ | rotor specific work |
| $\alpha$ | absolute flow angle |
| $\alpha_\infty$ | angle of mean absolute flow |
| $\beta_M$ | profile stagger angle |
| $\beta_\infty$ | angle of mean relative flow |
| $\Gamma$ | circulation |
| $\Delta c_u$ | absolute circumferential velocity variation |
| $\Delta w_u$ | relative circumferential velocity variation |
| $\Delta p_T$ | total fan pressure |
| $\Delta t$ | timestep |
| $\gamma$ | angle describing the sweep |
| $\varepsilon$ | slip coefficient; swirl coefficient |
| $\eta$ | total efficiency of the axial fan |
| $\eta_f$ | leakage performance |
| $\eta_h$ | hydraulic performance |
| $\nu$ | hub-to-tip ratio |
| $\phi$ | flow coefficient |
| $\psi^*$ | pressure coefficient |
| $\Omega$ | rotor angular speed |

## 1. INTRODUCTION

Axial fans are present in many industrial, commercial, and residential applications. Some applications include air conditioning and ventilation systems, cooling systems of electronic component, automotive or stationary internal combustion engines, electric motors, etc. Consequently, there is a continuous demand to improve their performance through more efficient designs.

However, since axial fan rotors are an intense source of noise, especially in industrial fans, noise reduction should become one more essential and indispensable objective in the design steps.

Therefore, it is essential that new projects aim to improve aerodynamic performance and to reduce noise emissions from this type of fan.

The aeroacoustics design of axial fans plays an important role in controlling their sound emission level and preserving their aerodynamic performance.

In this sense, the aim of this work is to present the design methodology for low-speed axial fan rotors considering the conditions of free vortex (FV) and non-free vortex (NFV). Both conditions were evaluated with the incorporation of the blades displacement in the circumferential direction in the same direction of rotation of the rotor in order to analyze the aeroacoustics behavior through CFD techniques.

Literature review shows that the incorporation of the forward sweep of the blade is beneficial for rotors with a non-free vortex design (Vad, 2011, 2012; Vad *et al.* 2015 and Masi *et al.* 2016). The sweep effect in rotor designs with a non-free vortex design contributes to the attenuation of the radial component of the flow which reflects in the reduction of losses caused by the flow separation, an efficiency improvement, and noise reduction. The authors outline that the gains in aerodynamic behavior (moderation of the total pressure loss on the suction side and, consequently, efficiency gain) can be explained since the sweep influences the behavior of the flow between the blades. The authors also emphasize that with the incorporation of the sweep, the streamlines are closer to being perpendicular to the leading edge and the trailing edge (with an appropriate sweep angle), causing the flow path along the blade surface to be shorter. This results in lower losses since the boundary layer on the suction side of the blade becomes thinner.

Axial flow fans with forward sweep in the circumferential direction compared to fans with the backward sweep, have a higher efficiency in the usual operating range (close to the design point). Also, resulting in a substantially lower noise emission. However, if the fan operates under off-design conditions the fan with a backward sweep would have a lower sound emission than the fan with a forward sweep (Krömer and Becker, 2018).

Carolus and Beiler (1997), Beiler and Carolus (1999) and Zenger and Becker (2016) have verified that with the sweep forward, the mean axial velocity increases in the hub region (which is generally threatened by the flow separation) and decreases in the tip region. This results in a stabilization of the flow field during the passage through the fan rotor and, consequently, a velocity profile at the outlet more regular than in the case of the rotor with backward sweep. As a consequence, the forward circumferential sweep leads to a decrease in the unstable blade forces and, hence, to a reduction in the level of tonal peaks in the blade passage frequency and its harmonics. Fans with forward sweep weaken the tip vortex formation due to the modification in blade loading and thus they reduce the noise of the blade tip (Krömer *et al.* 2019).

## 2. DESIGN METHODOLOGY

Conventional and validated methodologies were considered for the preliminary design of axial flow fans. They included the application of the lift wing theory, the free vortex and non-free vortex condition and the radial equilibrium equation.

Additionally, we proposed to incorporate the forward sweep effect on the blades in the circumferential direction defined through a cubic function.

### 2.1 Theoretical fundamentals of linear cascades

Figure 1 a) represents a linear cascade typical of an axial rotor since a linear cascade is a cylindrical cutting and development in a cascade radius station.

As an approximation, it is assumed that the fluid will flow on that cylindrical surface of radius, $r$, without considering the radial component of velocity. The spacing between two consecutive profiles is called pitch (blade spacing), $t$, the chord length of each profile is denoted by $l$, and the stagger angle of these profiles in relation to the circumferential direction is called $\beta_M$. The flow approaches the cascade with relative velocity, $w_3$, considered uniform in the inlet section. The flow when deflected by the profiles moves away from the cascade with relative velocity, $w_6$, is also considered uniform in the exit section.

Two-dimensional, steady state (in relation to the moving linear cascade), incompressible and non-viscous flow is also allowed. The development that follows has also been presented by the works of Albuquerque (2006), Sarmiento (2013) and Mota (2018).

Figure 1(b) shows the details of the velocity triangles at the inlet (with non-swirl of the absolute flow at the inlet) and at the outlet, where the relative flow mean velocity (of flows on the input, $w_3$, and the output of the cascade, $w_6$) of relative flow, $w_\infty$, is defined by: $\vec{w}_\infty = (\vec{w}_3 + \vec{w}_6)/2$.

The lift force, $F_L$, that the flow exerts on the profile (which is most responsible for the transfer of energy between the fluid and the blade) is due to the development of a circulation, $\Gamma$, around the profile.

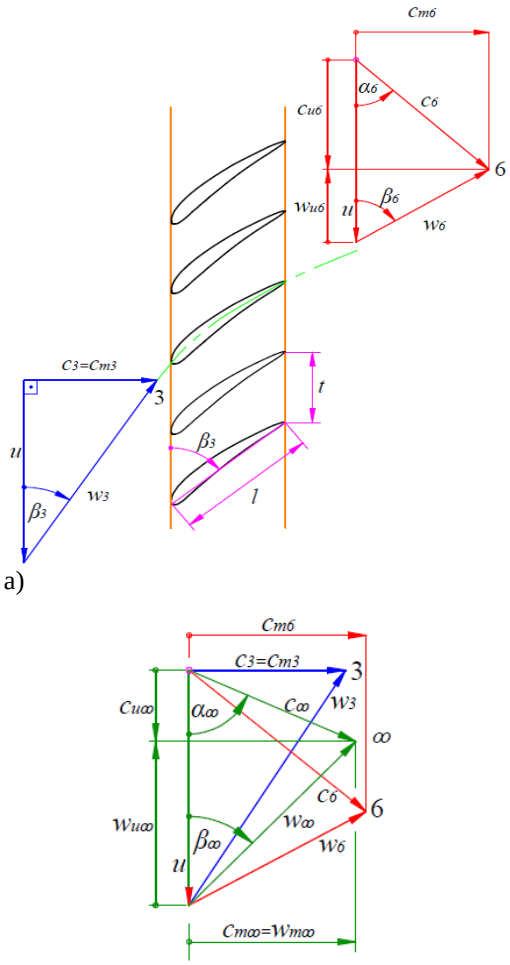


**Fig. 1. a) linear cascade; b) Velocity triangles with non-swirl of the absolute flow at the inlet.**

It can be demonstrated in Eck (1973) that this circulation is:

$$\Gamma = w_{u3}\,t - w_{u6}\,t = t\,\Delta w_u = t\,\Delta c_u\,, \tag{1}$$

where $\Delta c_u$ is the difference in components of the absolute velocity in the circumferential direction, given by $\Delta c_u = c_{u6} - c_{u3}$.

Applying the momentum equation in integral form to the control volume that involves a profile and using the Bernoulli equation for the rotor, it is possible to determine the circumferential ($u$) and axial ($z$) components of the force that the blade exerts on the fluid and vice versa. These force components are (Eck, 1973):

$$F_{B_u} = \rho\, w_{m\infty} bt(w_{u3} - w_{u6}) = \rho\, w_{m\infty} bt\frac{\Gamma}{t} = b\rho\, w_\infty \Gamma \operatorname{sen}\beta_\infty$$

and $F_{B_z} = \rho(w_{u3} - w_{u6})t\,b\,w_{u\infty} = b\,\rho\, w_\infty \Gamma\cos\beta_\infty$.

Where $t$ is the pitch, and $b$ is the blade span.

The result of these two components is the force on the blade, $F_B$, whose module is:

$$F_B = b\rho\, w_\infty \Gamma \tag{2}$$

The force on the blade, acts perpendicular to the mean relative flow velocity, $\vec{w}_\infty$, in the case of ideal flow, where, $F_B \approx F_L$ (Fig. 2).

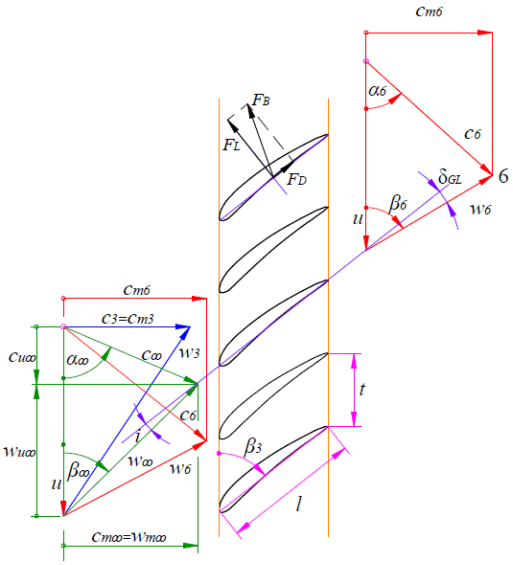


**Fig. 2. Lift and drag forces on a linear cascade profile.**

The previous results correspond to the well-known Kutta-Joukowsky theorem that, for the case of linear cascade, can be stated as: "The force $\vec{F}_B$ due to a potential, incompressible and steady state flow over a profile arranged in a linear cascade is perpendicular to the mean velocity vector, $\vec{w}_\infty$". The intensity of this force, per unit of blade height, $b$, is given by Eq. (3), where $\rho$ is the density of the fluid operated by the turbomachinery and $\Gamma$ is the circulation around the profile.

$$F_B / b = \rho\, w_\infty \Gamma\,, \tag{3}$$

The velocity that plays the role of incident velocity on a lift wing for the flow around an axial turbomachine blade profile is the mean velocity $\vec{w}_\infty$. Figure 2 represents the situation for the case of generating turbomachine, where $i$ is called the incidence angle (angle between $\vec{w}_\infty$ and the direction of the length chord of the profile), and the profile stagger angle is calculated by $\beta_M = \beta_\infty + i$.

In the ideal flow, the force on the blade, $\vec{F}_B$, is the lift force, $F_L$, which is the only force acting on the blade and acts perpendicular to the mean relative flow velocity, $\vec{w}_\infty$.

In the real flow, due to the viscous effects, a component of force appears parallel to $\vec{w}_\infty$, so that $\vec{F}_B$ becomes the resultant of two forces components, as shown in Fig. 2. This component parallel to $w_\infty$ is called the drag force, $F_D$. In an aerodynamic profile design, the purpose is to seek the lowest possible values for this coefficient, within the normal operating range of the

turbomachinery. Thus, $F_D << F_L$, obtaining the slip coefficient $tan\varepsilon = F_D/F_L \approx \varepsilon$. This coefficient depends on the profile geometry and the incidence angle, as well as the lift and drag forces.

As mentioned before, there is only lift if a non-zero circulation is created around the profile (Kutta-Joukowsky theorem), therefore, the profile geometry and its arrangement in the incident flow must be such that the necessary circulation takes place.

Circulation or lift, can be obtained through the camber line of the profile and the incidence angle, *i*.

Considering an aerodynamic profile arranged in an incompressible flow with uniform relative velocity, $\vec{w}_\infty$, and with incidence angle, *i*, the dimensionless lift and drag coefficients are, $C_L = F_L/((1/2)\rho w_\infty^2 \ell)$, $C_D = F_D/((1/2)\rho w_\infty^2 \ell)$, respectively.

### 2.2 Resulting condition of the wing theory and cascade theory

The following equation is obtained considering the effect of circulation, $\Gamma$, the blade force, the lift coefficient and under the assumption that $F_D \approx F_L$ in the optimal operating region of the profiles:

$$F_L = b\rho w_\infty t \Delta c_u = 1/2(bC_L\rho w_\infty^2 \ell) \tag{4}$$

or

$$C_L \frac{\ell}{t} = \frac{2\Delta c_u}{w_\infty} \tag{5}$$

The Eq. (5) forms the basis for calculation the blade of axial turbomachinery rotors through lift wing theory. In this equation, quantities from the flow velocity triangles are related to the desired dimensionless characteristics for the cascade profiles. This is very important in the aerodynamic design of the cascade of the axial turbomachine rotor and stator.

### 2.3 Radial equilibrium condition

The momentum equation (Navier-Stokes equation) in the radial direction is also known as the radial equilibrium equation. For three-dimensional, unsteady, viscous flow, the momentum equation in the radial direction can be written in cylindrical coordinates (Yahya, 1983), as follow (Eq. 6):

$$c_r \frac{\partial c_r}{\partial r} + \frac{c_u}{r}\frac{\partial c_r}{\partial \theta} + c_a \frac{\partial c_r}{\partial z} - \frac{c_u^2}{r} + \frac{\partial c_r}{\partial t} - F_c + \frac{1}{\rho}\frac{\partial p}{\partial r} = \frac{\mu}{\rho}\left(\frac{\partial^2 c_r}{\partial r^2} + \frac{1}{r}\frac{\partial c_r}{\partial r} - \frac{c_r}{r^2} + \frac{1}{r^2}\frac{\partial^2 c_r}{\partial \theta^2} - \frac{2}{r^2}\frac{\partial c_u}{\partial \theta} + \frac{\partial^2 c_r}{\partial z^2}\right)$$

Assuming a flow with axial symmetry, steady state, non-viscous and disregarding field forces, $F_c$, Eq. (6) becomes

$$c_r \frac{\partial c_r}{\partial r} + c_a \frac{\partial c_r}{\partial z} - \frac{c_u^2}{r} = -\frac{1}{\rho}\frac{\partial p}{\partial r} \tag{7}$$

In radial equilibrium, the radial component of velocity is neglected, $c_r=0$ and a purely axial flow is assumed in the meridional projection, therefore:

$$\frac{c_u^2}{r} = \frac{1}{\rho}\frac{\partial p}{\partial r} \tag{8}$$

To determine the distribution of axial velocities ($c_m = c_a$) in the radial direction in axial turbomachinery, the Eq. (8) can be solved in two ways:

In the first way, the condition of free vortex or potential vortex is adopted. This formulation is commonly used in hydro or aerodynamic design of axial turbomachinery. In this approach, also presented in Albuquerque (2006) and Bran and Souza (1969), the Bernoulli equation applied to the rotor is considered constant:

$$p/\rho + w^2/2 - u^2/2 = \text{Constant} \tag{9}$$

As the radial component of velocity is neglected, streamlines are implicitly parallel to the machine axis (reasonable as a first approach on an axial rotor) and hence, $u = \omega r$ is supposed to be constant along a given streamline.

Equation (10) can be obtained from the velocity triangles and the Euler equation of the axial turbomachinery:

$$Y_B = u\,\Delta c_u \tag{10}$$

to finally get Eq. (11) for Free-Vortex condition:

$$c_m = c_a = \text{const.} \Leftrightarrow Y_B = \text{const.} \Rightarrow r\,c_u = \text{const.} \tag{11}$$

Equation (11) shows that if $c_m = c_a$ is constant along the length of the blade, then, $Y_{Blade}$ it is also constant along the blade and vice versa.

The second way of solving the Eq. (8), is to adopt certain types of non-free vortexes as described in Yahya (1983), for the blade design. In these methodologies, both $Y_B$ and $c_m$ are no longer constant along the height of the blades.

This work will use a type of non-free vortex based on Wallis (1983) and Sarmiento *et al.* (2017), where the circumferential component of the absolute velocity after the rotor, $c_{u6}$, varies linearly along the blade. This condition is represented by Eq. (12).

$$\varepsilon_6 = c_{u6}/\bar{c}_a = a + bx \tag{12}$$

where $\varepsilon_6$, is the swirl coefficient of the absolute flow at the rotor outlet, and

$$x = r/r_e \tag{13}$$

with $r_i \le r \le r_e$, *a* and *b* constants to be determined. The main reason for choosing the non-free vortex condition, is because it works with relatively low hub-to-tip ratio, *v*, which are typical of low-pressure axial fans that, in general, present hub-to-tip ratio less than 0.3. If the free-vortex condition was used for these hub-to-tip ratios, it would result in a strong twist of the blades in the region close to the blade root, which implies very strong swirl near the hub and flow separation in this region,

and consequently a less uniform axial outlet velocity distribution, thus influencing the aerodynamic performance characteristics, as described in Dachuan *et al.*, (2019) and in Vad (2011).

Thus, disregarding the gravitational effect and differentiating Eq. (9) it becomes:

$$dp/\rho + dw^2/2 = 0\,, \tag{14}$$

Combining Eq. (8) and Eq. (14), results in

$$2\frac{c_u^2}{r}dr = dw^2 \tag{15}$$

Dividing the two sides of Eq. (15) by the mean meridional component of the absolute velocity along the blade squared, $\overline{c}_a^2$ and multiplying and dividing the right side by $r_e$, results in Eq. (16).

$$2\int_{x_0}^{x}\frac{\frac{c_{u6}^2}{\overline{c}_a^2}}{\frac{r}{r_e}}d\left(\frac{r}{r_e}\right) = \int_{x_0}^{x} d\left(\frac{w_3^2}{\overline{c}_a^2} - \frac{w_6^2}{\overline{c}_a^2}\right) \tag{16}$$

with, according to the velocity triangles of Fig. 1,

$$w_3^2 = w_{a3}^2 + w_u^2 = c_{a3}^2 + u^2 \tag{17}$$

(Since $\alpha_3 = 90^0$ and $w_{a3} = c_{a3}$)

$$\begin{aligned} w_6^2 &= w_{a6}^2 + w_{u6}^2 = c_{a6}^2 + (u - c_{u6})^2 \\ &= c_{a6}^2 + u^2 - 2uc_{u6} + c_{u6}^2 \end{aligned} \tag{18}$$

(Since $w_{a6} = c_{a6}$)

Therefore,

$$w_3^2 - w_6^2 = c_{a3}^2 - c_{a6}^2 + 2uc_{u6} - c_{u6}^2 \tag{19}$$

Dividing all the terms of the Eq. (19) by the mean meridional component of absolute velocity along the blade squared, $\overline{c}_a^2$, results in Eq. (20),

$$\frac{w_3^2}{\overline{c}_a^2} - \frac{w_6^2}{\overline{c}_a^2} = \frac{c_{a3}^2}{\overline{c}_a^2} - \frac{c_{a6}^2}{\overline{c}_a^2} + \frac{c_{u6}}{\overline{c}_a}\left(\frac{2u}{\overline{c}_a} - \frac{c_{u6}}{\overline{c}_a}\right) \tag{20}$$

Substituting Eq. (20) in Eq. (16), and using Eq. (12), the Eq. (21) is obtained:

$$\begin{aligned} &2\int_{x_0}^{x}\varepsilon_6^2\frac{dx}{x} = \\ &= \int_{x_0}^{x} d\left[\left(\frac{c_{a3}}{\overline{c}_a}\right)^2 - \left(\frac{c_{a6}}{\overline{c}_a}\right)^2 + \frac{c_{u6}}{\overline{c}_a}\left(\frac{2u}{\overline{c}_a} - \frac{c_{u6}}{\overline{c}_a}\right)\right] \end{aligned} \tag{21}$$

Considering that the flow coefficient is defined by:

$$\phi = \overline{c}_a/u \tag{22}$$

And using the Eq. (22) and (12), the Eq. (21) becomes, after integrating the second member into Eq. (23).

$$\begin{aligned} \left(\frac{c_{a6}}{\overline{c}_a}\right)_x^2 &= \left(\frac{c_{a6}}{\overline{c}_a}\right)_{x_o}^2 + \left[\varepsilon_6\left(\frac{2}{\phi} - \varepsilon_6\right)\right]_x \\ &- \left[\varepsilon_6\left(\frac{2}{\phi} - \varepsilon_6\right)\right]_{x_o} - 2\int_{x_o}^{x}\varepsilon_6^2\frac{dx}{x} \end{aligned} \tag{23}$$

The approximate solution of the momentum equation, Eq. (8), along of the blade span, considering that there is no swirl of the absolute flow at the inlet of the rotor (without pre-rotation), that is, $c_{u3} = 0$, can be obtained, by Eq. (23).

In Eq. (23), $x_o$ represents a fixed value of $x$ (for a given rotor design) that must be obtained by an iterative process, in order to comply with the condition given by Eq. (24).

$$\overline{c}_{a3} = \overline{c}_{a6} = \overline{c}_a \tag{24}$$

Recalling that in Eq. (24) it is assumed that the flow is incompressible and purely axial, with the inlet section equal to the outlet section, this is no contraction of the duct segment across the rotor.

Considering Eq. (24) and because the meridional (axial) component of the absolute velocity at the rotor outlet, $c_{a6}$, is considered be equal to $\overline{c}_a$ in the radial section $x_o$, the first term on the right side of Eq. (23) becomes:

$$\left(c_{a6}/\overline{c}_a\right)_{x_o}^2 = 1 \tag{25}$$

The last term on the right side of Eq. (23) is obtained through analytical integration, this results in:

$$\begin{aligned} &2\int_{x}^{x}\varepsilon_6^2\frac{dx}{x} = 2\int_{x_o}^{x}(a+bx)^2\frac{dx}{x} \\ &= \left[2a^2\ln x + b^2x^2 + 4abx\right]_x \\ &- \left[2a^2\ln x + b^2x^2 + 4abx\right]_{x_o} \end{aligned} \tag{26}$$

The value of $x_o$ (radial section where $c_{a6}/\overline{c}_a$ is equal to *1*) is determined based on Eq. (27) according to the integral continuity equation, that is, $\dot{V}_R = \overline{w}_m A = \overline{c}_m A = \overline{c}_a A$, then,

$$\overline{c}_a = \overline{c}_{a6} = \frac{1}{A}\int_{r_i}^{r_e} c_{a6}dA = \left\{1\Big/\left[\pi\left(r_e^2 - r_i^2\right)\right]\right\}\int_{r_i}^{r_e} c_{a6}2\pi r dr$$

or

$$\frac{\overline{c}_{a6}}{\overline{c}_a} = \left\{1\Big/\left[\pi\left(\frac{r_e^2}{r_e^2} - \frac{r_i^2}{r_e^2}\right)\right]\right\}\int_{r_i/r_e}^{r_e/r_e}\frac{c_{a6}}{\overline{c}_a}2\pi\frac{r}{r_e}d\left(\frac{r}{r_e}\right),$$

therefore,

$$\frac{\overline{c}_{a6}}{\overline{c}_a} = \frac{1}{1 - x_i^2}\int_{x_i}^{1}\frac{c_{a6}}{\overline{c}_a}x\,dx = 1 \tag{27}$$

The value of $x_o$ is established when $\overline{c}_{a6}/\overline{c}_a$, calculated according to Eq. (27) produces a value equal to *1* (one) or very close to *1*, by means of an iterative process. The integral solution in Eq. (27)

can be obtained by numerical integration (quadrature). The quadrature used in the computer program is that of Gauss-Legendre.

The iterative process for determining the value of $x_o$ is summarized below:

1) The $x_o$ value is adopted in the range $x_i < x_o < 1$, preferably a value closer to the hub, $x_i$, than to the blade tip, $x_e = 1$.

2) Calculate the value of $\varepsilon_6 = a + bx$, with this value of $x_o$. The constants $a$ and $b$ are obtained from two points on the curve $\varepsilon_6 = \varepsilon_6(x)$ which represents the distribution of $\varepsilon_6$ for the free vortex condition. A point is that referring to the blade tip with ordinates $(x, \varepsilon_6) = (1, \varepsilon_{6t})$ where $\varepsilon_{6t}$ is the value of $\varepsilon_6$ at the blade tip. The other point is that corresponding to the value of $x_o$ (adopted) with ordinates $(x, \varepsilon_6) = (x_o, \varepsilon_{6x_o})$ where $\varepsilon_{6x_o}$ is the value corresponding to $x_o$ taken from the free-vortex condition. See Fig. 3.

3) Determining the linear dependence of $\varepsilon_6 = \varepsilon_6(x)$, that is, $\varepsilon_6 = a + bx$. Is calculated the expression $c_{a6} / \bar{c}_a$, Eq. (23), that represent the velocity distribution, which with other parameters, it depends on the distribution of $\varepsilon_6$, which in turn depends on $x_o$.

4) Once the velocity distribution is determined $c_{a6} / \bar{c}_a$, the mean value is calculated $\bar{c}_{a6} / \bar{c}_a$ and obtained by integration in the interval $x_i < x_o < 1$, according to Eq. (27).

5) If $\bar{c}_{a6} / \bar{c}_a = 1$, the correct value of $x_o$ was found; if $\bar{c}_{a6} / \bar{c}_a \neq 1$, another $x_o$ value must be adopted and repeat Items 1 to 4 above until $\bar{c}_{a6} / \bar{c}_a = 1$.

Figure 3 illustrates, the distribution of the swirl coefficient of absolute flow at the blade outlet, $\varepsilon_6$, and the ratio of axial (meridional) velocities at the rotor outlet, $c_{a6} / \bar{c}_a$ , for the free vortex condition (FV) and non-free vortex condition (NFV) along the length of the blades.

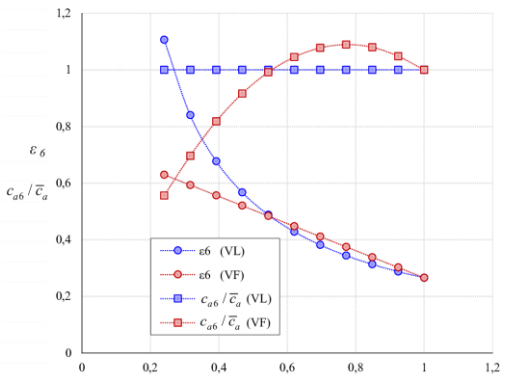


**Fig. 3. Distributions of $\varepsilon_6$ and $c_{a6} / \bar{c}_a$ along the length of the blades.**

### 2.4 Radial equilibrium condition

The discretized 3D points required to generate the profile coordinates, the radial stacking and the displacement in the circumferential direction (sweep) are determined for the preliminary design of the rotors through a Fortran® program code. For the project, operational data were considered regarding: 1) total fan pressure, $\Delta p_T$, 2) fan flow, $\dot{V}$ , 3) rotor rotation, $n$, and 4) density of the fluid operated by the fan, $\rho$. See Table 1.

**Table 1 Design conditions of the axial fan rotors**

| $\dot{V}$ | $\Delta p_T$ | $\rho$ | $n$ | $N$ | $D_e$ |
|---|---|---|---|---|---|
| m$^3$/s | Pa | kg/m$^3$ | rpm | - | mm |
| 1.9 | 137.34 | 1.225 | 1800 | 8 | 500 |

With the values of $\Delta p_T$, $\dot{V}$ and $n$, is obtained the specific rotation value: $n_{qA}=n\dot{V}^{1/2}/(\Delta p_T / \rho)^{3/4}\times 10^3$, and another quantities.

If there is no swirl of the absolute flow at the rotor inlet, therefore $c_{u3} = 0$, the Euler equation of the turbomachinery for the case of axial fans in the real condition is given by:

$$Y_B = u\,\Delta c_u = u\left(c_{u6} - c_{u3}\right) = u\,c_{u6} \tag{28}$$

As shown in the radial equilibrium section, the radial component of absolute velocity is $c_r = 0$, therefore the meridional component of absolute velocity, $\vec{c}_m = \vec{c}_r + \vec{c}_a$, becomes $c_m = c_a$.

The specific work of the rotor in the real condition, $Y_B$, can be set as a function of $\phi$ (flow coefficient) and $\varepsilon_6$ (swirl coefficient at the rotor outlet), that is,

$$\frac{Y_B}{\bar{c}_a^2} = \frac{u}{\bar{c}_a}\frac{c_{u6}}{\bar{c}_a} = \frac{\varepsilon_6}{\phi} = K_{VL} \tag{29}$$

Both $\phi$ and $\varepsilon_6$ in the radial direction (vary along the length of the blades), since $u$ and $c_{u6}$, vary in the radial direction.

In the case of free vortex (FV), both $Y_B$ and $c_a = c_{a3} = c_{a6} = \bar{c}_a$ are constant in the radial direction. Based on Eq. (29), it can be defined a pressure coefficient, $\psi_B^*$, according to the Eq. (30).

$$\psi_B^* = \frac{\Delta p_{T\,B}}{\frac{1}{2}\rho\bar{c}_a^2} = \frac{\Delta p_T}{\frac{1}{2}\rho\bar{c}_a^2\eta_h} = \frac{2Y_B}{\bar{c}_a^2} = 2\frac{u}{\bar{c}}\frac{c_{u6}}{\bar{c}} = \frac{2\varepsilon_6}{\phi} \tag{30}$$

In the case of free vortex (FV) $\psi_B^*$ is constant in the radial direction, but $\psi_B^*$ will not be constant for non-free vortex (NFV) in the radial direction.

The flow of the rotor, $\dot{V}_R$, in terms of the fan flow, $\dot{V}$ , is related to the leakage performance by

$$\dot{V}_R = \dot{V}/\eta_f \tag{31}$$

The rotor flow, without considering the thickness of the blades, is given by

$$\dot{V}_R = \bar{c}_m A = \bar{c}_m \pi \left(r_e^2 - r_i^2\right) = \bar{c}_a \pi \left(r_e^2 - r_i^2\right) \quad (32)$$

where $r_i$ and $r_e$ are the polar radius referring to the hub and the tip of the blade respectively.

Therefore, the mean axial component of absolute velocity is given by the Eq. (33).

$$\bar{c}_a = 4\dot{V}_R \Big/ \pi \left(r_e^2 - r_i^2\right) \quad (33)$$

The mean meridional velocity of the relative flow, $w_m$, it can be also written as $w_m = w_a = c_m = c_a$.

The value of the diameter ratio, $\nu$, is also calculated through diagrams for pre-dimensioning of axial fan rotors. Thus, the internal diameter of the rotor is obtained by: $D_i = \nu D_e$.

Then, a number of radial sections of diameter $D$ are adopted in the range $D_i \leq D \leq D_e$ and the circumferential velocities, $u = \pi D n$, are calculated in each radial section.

Then, the following guide was adopted, initially calculating some quantities for the free-vortex condition, for each radial section of the blades:

(a) Component of absolute velocity in the circumferential direction at the rotor outlet;

$$c_{u6} = \Delta c_u = Y_{Blade}/u \quad (34)$$

Where, $c_{u6} = \Delta c_u$ by the fact that $c_{u3} = 0$.

(b) Flow coefficient, $\phi$, and swirl coefficient of absolute flow at the rotor outlet, $\varepsilon_6$, by Eq. (35):

$$\varepsilon_6 = c_{u6}/\bar{c}_a = \psi^* \phi / 2\eta_h \quad (35)$$

The absolute swirl coefficients at the rotor outlet, and the flow coefficient at the tip of the blade, $\varepsilon_{6t}$, $\phi_t$, respectively, are necessary quantities for the iterative process of non-free vortex.

(c) Constant value, $k_{FV}$, in free vortex condition,

$$k_{FV} = \varepsilon_6/\phi = \psi^*/2\eta_h \quad (36)$$

(d) Then, the iterative process for the non-free vortex condition continues until the value of $x_o$ is found, for which the ratio of axial (meridional) velocity at the rotor outlet is equal to *1* ($\bar{c}_{a6}/\bar{c}_a = 1$). Thus, it is possible to obtain the distribution of the swirl coefficient at the outlet of the blades, $\varepsilon_6$, and the ratio of axial velocity at the rotor outlet, $\bar{c}_{a6}/\bar{c}_a = 1$, for the free-vortex and non-free vortex condition along the length of the blades.

(e) Velocity triangles for point *3* and *6* can be completely defined once the distributions of the swirl coefficient at the blade outlet, $\varepsilon_6$, and the ratio of axial velocities at the rotor outlet, $\bar{c}_{a6}/\bar{c}_a = 1$, are known.

(f) The values of $C_L\,(l/t)$ are obtained from Eq. (5).

(g) Solidity ratios are calculated (chord-pitch ratios), $l/t$. For the calculation of the chord, $l$, values of the ratio between the blade height and the chord, $h/l$ were adopted. Usually, values of $h/\ell$, in the range 3 to 5 are being recommended. Ratios between the tip-chord and root-chord, $l_{Tip}/l_{Root}$, in the range of 0.2 to 1, are being recommended for incompressible flow.

(h) The pitch ($t = \pi D/N$) and chords are calculated.

(j) The lift coefficients, $C_L$ ($C_L = (C_L\,(\ell/t)/\ell/t)$);

(k) The maximum thicknesses, $e_{max}$, are estimated for material strength requirements. In this evaluation, a combined effect of stresses can be considered: normal stresses due to the bending moment, caused by the lift forces, $F_L$, and normal stresses due to the centripetal force on the rotating blades. Hence, thicknesses can be estimated by specifying an allowable stress value for the material. Another procedure considered valid for the preliminary design, is to adopt a typical value of relative thickness, ($e_{max}/l$) for axial fans, and based on the value of the chords for each radial section previously calculated, determine the maximum thickness. In this work, the last procedure is considered.

(l) The relative thicknesses, $e_{max}/l$;

(m) Profiles are chosen for each radial section with the aid of polar diagrams ($C_D \times C_L$). We aim to search the polar curves for those profiles that with the support coefficient determined in (j) present slip coefficients close to $\varepsilon_{min}$. That is, for each $C_L$ value, look for a profile that, at this point, has little $tg\varepsilon = (C_D/C_L)$. Thus, the Gottinger GÖ 480 profile was obtained from the polar diagram. Suzuki *et al.* (1985) previously analyzed the effect of pressure distribution along the blade and came to the conclusion that a blade profile with modified Gottinger profiles produced less noise broadband in the high frequency region. The authors explain that this is because the pressure distribution on the suction side of this type of profiles is smoother and lift fluctuation is small.

(n) The constants $a$ and $b$ of the correlation $C_L = C_L(y_{\max}/\ell, \delta) \approx a\, y_{\max}/\ell + b\, i$ (Bran and Souza, 1969) are sought and the incidence angles are calculated once the profiles are established. In the previous correlation, $y_{max}$ is the maximum thickness and $i$ is the incidence angle. The incidence angles should reduce in a smooth manner from the root to the tip of the blade. Negative or large values (close to the profile stall) reflect inappropriate choices for profiles.

(o) The stagger angle of the blades, $\beta_M = \beta_\infty + i$;

(p) The thinning coefficients $C_0 = (y_{max}/l)/(y_{max}/l)b$ are used to calculate the thicknesses of the profiles that make up the blades as a function of the thicknesses of the root profile.

(q) Reynolds Numbers, slip coefficients ($\varepsilon = C_D/C_L$), and degrees of reaction ($\tau = 1 - c_{u6}/(2u)$) are obtained.

Therefore, it will be possible to obtain the two-dimensional coordinates (*x*, *y*) of each radial sections of the preliminary geometry of the axial flow fan rotor with the above presented procedure. The profiles will then be rotated with the respective stagger angle for each radial section, for which the axis rotation concept is used.

### 2.5 Circumferential sweep

Some authors showed that a non-uniform distribution of the sweep angle in the radial sections, with a more accentuated sweep at the blade tip, can be beneficial in the behavior of axial fans (Wadia *et al.* 1998; Corsini and Rispoli 2004; Masi and Lazzaretto 2017; Herold *et al.* 2017; Krömer and Becker 2018; Krömer *et al.* 2019).

For instance, in Yang (2016) the stacking line is composed of a straight line, up to approximately 40% of the height of the blade (starting from the root) and an arc of a circle in the region near the tip.

In another one (Masi *et al.* 2018), they compared a fan with a forward sweep with a more pronounced sweep increase at the tip, with respect to a fan with uniform sweep (linear increment). They reported that the efficiency of the rotor showed an increase in the entire operating range for the fan with sweep forward marked in the region near the tip.

Thus, in this work, a distribution of sweep angles based on a cubic function is proposed. This would allow better control of the sweep angle in the blade tip. See Fig. 4.

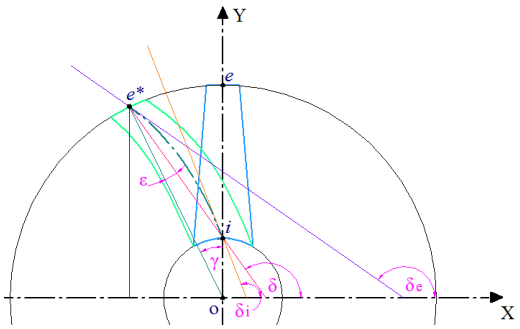


**Fig. 4. Geometric parameterization for variations of circumferential sweep of blade.**

As shown in Fig. 4, the development of the circumferential sweep effect can be described by the following conditions:

- The blade rotation in a counterclockwise direction is characterized by the $\gamma$ angle.

- The stacking line is taken at 50% of the leading edge of each blade profile (*i*-*e*) coinciding with the *y-axis* of the Cartesian coordinate system.

- The stacking line with circumferential sweep ($i-e^*$) is described by a cubic function, Eq. (37):

$$f(x) = ax^3 + bx^2 + cx + d \tag{37}$$

Adopting different conditions for the points *i*, *e**, and taking into account that the $\delta_i$ value must be in the interval $\pi/2 \le \delta_i \le \delta$, and the $\delta_e$ value must be in the interval $\delta \le \delta_e \le (\pi + \gamma)$, the cubic function constants are found:

$$a = \left\{2\left[r_e \cos\gamma + a_1 + a_2 - r_i\right]\right\} \Big/ \left(r_e^3 sen^3\gamma\right)$$
$$a_1 = 0.5 r_e \tan\delta_i \, sen\gamma \tag{38}$$
$$a_2 = 0.5 r_e \tan\delta_e \, sen\gamma$$

$$b = \left(3a\, r_e^2 sen^2\gamma + \tan\delta_i - \tan\delta_e\right) \Big/ \left(2 r_e sen\gamma\right) \tag{39}$$

$$c = \tan\delta_i \tag{40}$$

$$d = D_i/2 \tag{41}$$

The angles $\gamma$, $\delta_i$, $\delta_e$ and the hub-to-tip ratio were studied through a parametric variation.

The angle $\gamma$, defines the rotation of the blade tip, from point *e* to point *e** in a counterclockwise direction, ranging from 15° to 25°.

The angles $\delta_i$ and $\delta_e$ formed between the *x* ordinate and the tangents to points *i* and *e** vary, respectively, from 100° to 115° in the case of angle $\delta_i$, and from 120° to 150° in case of angle $\delta_e$. These angles were chosen in such a way that the specific angle of the sweep varies from 0° in the root, to approximately 60° at the blade tip, according to the studies reported in the literature.

Therefore, at first three cubic functions (functions $f_1$, $f_2$ and $f_3$) were studied as reported in Table 2 and outlined in Fig. 5.

**Table 2 Cubic function parameters that defines the centerline of the circumferential sweep**

| | $\gamma$ | $\delta_i$ | $\delta_e$ |
|---|---|---|---|
| $f_1$ | 15º | 100º | 120º |
| $f_2$ | 25º | 115º | 135º |
| $f_3$ | 20º | 100º | 150º |

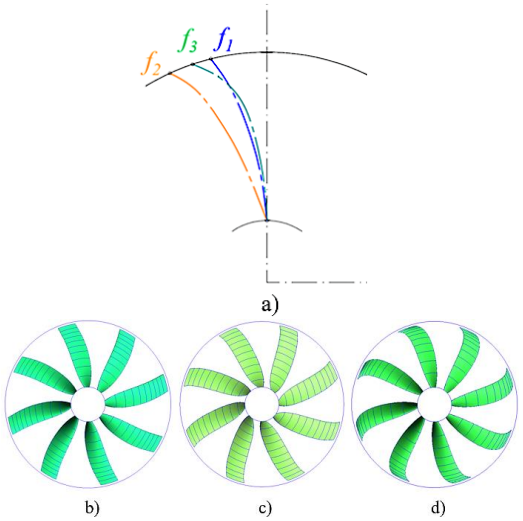


**Fig. 5. a) Sweep with cubic functions; b), c), d) Rotors with functions $f_1$, $f_2$ e $f_3$, respectively.**

In addition to the cubic function that controls the circumferential sweep, geometric shapes such as the hub-tip ratio, variations in chord distribution and thickness were also studied.

Table 3 shows the results of CFD analysis corresponding to the parametric variation, where the influence on hydraulic efficiency of the geometric parameters that control the cubic function of the sweep and other geometric parameters mentioned was evaluated. The hydraulic efficiency is defined as follow:

$$\eta_h = \frac{\Delta p_T \dot{V}}{M \Omega} \tag{42}$$

Where M in the moment, and the Ω is the angular velocity.

**Table 3 Parametric variation of blade geometry with circumferential sweep**

| *Fan* | ***f(x)*** | ***v*** | $l_{Tip}$ | $e_{Root}$ | $e_{Tip}$ | $\eta_h$ | $\Delta p_T$ |
|---|---|---|---|---|---|---|---|
| | - | - | mm | mm | mm | % | Pa |
| V-1 | $f_1$ | 0.21 | 55.3 | 8.1 | 6.3 | 73.85 | 103.81 |
| V-2 | $f_2$ | 0.21 | 55.3 | 8.1 | 6.3 | 79.85 | 105.59 |
| V-3 | $f_3$ | 0.21 | 55.3 | 8.1 | 6.3 | 84.70 | 130.12 |
| V-4 | $f_3$ | 0.21 | 69 | 8.1 | 8.1 | 85.03 | 153.92 |
| V-5 | $f_3$ | 0.24 | 69 | 8.1 | 8.1 | 86.22 | 153.07 |
| V-6 | $f_3$ | 0.24 | 69 | 8.1 | 6.2 | 87.05 | 135.94 |
| V-7 | $f_3$ | 0.24 | 69 | 5.1 | 5.1 | 87.20 | 156.20 |
| V-8 | $f_3$ | 0.24 | 69 | 8.1 | 4.1 | 87.92 | 157.67 |
| V-9 | $f_3$ | 0.24 | 45.6 | 8.0 | 3.1 | 88.26 | 155.88 |

According to this parametric variation analysis, the rotor that presented a better aerodynamic performance in terms of hydraulic efficiency (V-9 rotor of Table 3), was obtained with a more accelerated cubic function in the tip region, $f_3$. Thus, the geometric parameters for generating the rotor reference geometry are shown in Table 4.

**Table 4 Parameters to define the fan geometry**

| $D_e$ | $v$ | $l_{Root}$ | $l_{Tip}$ | $\gamma$ | $\delta_e$ | $\delta_i$ |
|---|---|---|---|---|---|---|
| mm | – | mm | mm | ° | ° | ° |
| 500 | 0.24 | 69 | 45.6 | 20 | 150 | 100 |

## 3. NUMERICAL SIMULATION

The flow field was modelled using the Reynolds Average Navier–Stokes equations coupled with a turbulence model. The ANSYS Fluent, a three-dimensional commercial solving package, was used for simulating the flow field. This software is a finite volume-based solver. As a finite-volume method, it satisfies strict global conservation by enforcing local conservation over control volumes that are constructed around each mesh vertex or node. This approach is widely used in turbomachinery, in research works, such as, Asghari *et al.* (2019) and Roffi *et al.* (2017), among others.

It is important to mention that for the numerical solution of the Navier Stokes equation, in addition to the finite volume method, there are also other methods that can be advantageous in terms of processing time, especially when they are integrated with optimization algorithms. To name a few briefly, for example the Boundary Element method, BEM, and the viscous-non-viscous interaction models, are methodologies with low processing time, as shown by the works presented by Camacho and Barbosa (2005), Camacho and Manzanares Filho (2005) and Castilho *et al.* (2016).

### 3.1 Generation of rotor geometry and mesh

The rotor geometries for the free vortex (FV) and for the non-free vortex (NFV) conditions were obtained through the computer program code developed in Fortran that provides an output file which can be interpreted by the commercial program ICEM CFD® through auxiliary files like Script.dat. This file contains the points that define the geometry of the profiles in 3D with the stagger angle for each station, the displacement in the circumferential direction, and the projection in cylindrical coordinates. Figure 6 shows the two geometries of the fan rotors.

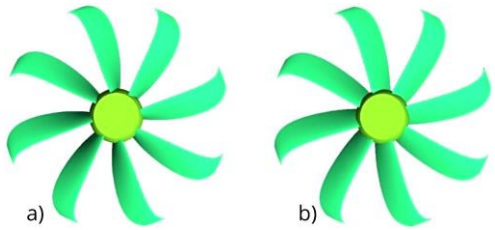


**Fig. 6. Axial fan rotor geometry: a) FV, b) NFV.**

Although the two rotors have the same distribution of thickness and chord length along the blade, the rotor FV has greater torsion at the blade root, due to the more pronounced stagger angles in this region.

### 3.2 Definition of computational domains and mesh generation

A cylindrical domain is considered for the simulation (in steady state). It is composed of the rotor subdomain, and a subdomain downstream of the rotor (Fig. 8). This approach is employed by Augustyn (2013) as well.

For the unsteady simulation, three domains were considered (Fig. 7): a semi-spherical domain upstream of the rotor, the rotor and a cylindrical domain in the region downstream of the rotor.

The parameters presented in Guédel *et al.* (2012) were taken as reference to determine the length of the computational domains and the boundary conditions.

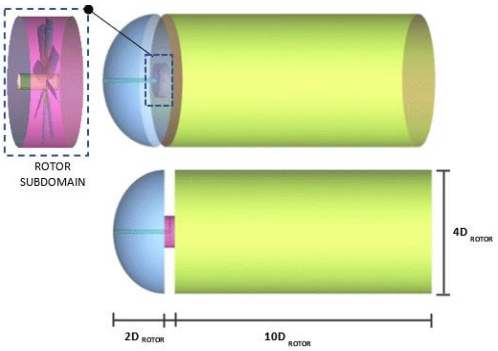


**Fig. 7. Simulation domain in the far field.**

A hybrid mesh of the tetrahedral type with hexahedral core and prismatic layer with 8 levels ($y^+ \sim 1$) on the surface of the blades was used in the rotor domain. This configuration controls the parameters related to the size and growth rates of the elements. This type of hybrid mesh reduces the number of elements considerably. The computational meshes were generated in the commercial program ICEM CFD®.

A hexahedral mesh was considered for the output domain of the simulation in steady state.

Then, a tetrahedral mesh with hexahedral core was considered for the downstream domain, in an unsteady state, in order to reduce the number of elements and consequently the computational cost.

To minimize the dependence of the results with the mesh refinement, preliminary simulations were considered for the design point of a rotor with forward sweep for mesh independence. For this, the number of elements is increased and its impact on results is measured. Similar approaches to mesh independence for turbomachinery, are presented in Aguirre *et al.* (2019), Sarmiento *et al.* (2020) and Sarmiento *et al.* (2021).

In this study, the percentage difference between the global magnitudes of the refined, coarse and reference meshes (less than 1%) was used to evaluate the mesh convergence, as follow:

$$\left| \left( \frac{\Delta p_{T\,ref} - \Delta p_T}{\Delta p_{T\,ref}} \right) \times 100 \right| \leq 1\% \tag{43}$$

$$\left| \left( \frac{\eta_{ref} - \eta}{\eta_{ref}} \right) \times 100 \right| \leq 1\% \tag{44}$$

The hydraulic efficiency and the total pressure value quantified in the rotor domain, between the inlet and outlet surfaces was used as an evaluation criterion. A reference mesh ($M_{ref}$), a coarse mesh ($M_1$) and a refined mesh ($M_2$) were considered.

In the initial mesh ($M_{ref}$) the number of elements is modified, mainly near the wall. According to Cox-Stouffer (1997), the first modified mesh ($M_1$) the number of elements must be reduced and in the second ($M_2$) a greater mesh refinement must be carried out. The results of the rotor mesh independence study can be found on Table 5.

**Table 5 Mesh independence parameters**

| Mesh | Elements number | $\Delta p_T$ | $\eta$ | $\varepsilon_{\Delta pT}$ | $\varepsilon_\eta$ |
|---|---|---|---|---|---|
| - | - | Pa | % | % | % |
| $M_1$ | 3 273 227 | 166.67 | 83.4 | - | - |
| $M_{ref}$ | 7 998 096 | 168.03 | 83.9 | 0.8 | 0.6 |
| $M_2$ | 8 935 016 | 168.66 | 84.3 | 0.3 | 0.5 |

The percentage differences of the global quantities considered with respect to the reference mesh are less than 1%. This means that these values do not vary significantly with a greater refinement of the mesh. Thus, the mesh satisfies the criterion of independence.

### 3.3 Boundary conditions

The *k-ω SST* (Shear Stress Transport) turbulence model was used for the steady state simulation. It is very suitable for flows that present high adverse pressure gradients and flow separation due to shear forces. This model integrates two widely used and robust models, the *k-ε* and *k-ω* models. These turbulence models depend mainly on the turbulent kinetic energy *k*, dissipation rate of the kinetic energy *ε*, turbulent frequency *ω* and the correlations between them. The *k-ω SST* model uses the formulation of the *k-ω* turbulence model, in regions close to the walls, where there is usually a low Reynolds Number that produces complex secondary flows and flow separations. The *k-ω SST* model changes to the use of the *k-ε* model formulation, in the presence of a high Reynolds Number in the regions most external to the domain walls, through the use of a mixing function that makes the activation in an appropriate way and selective use of these formulations without user intervention.

The boundary conditions imposed in the Fluent® program are shown in Fig. 8, and detailed as follow:

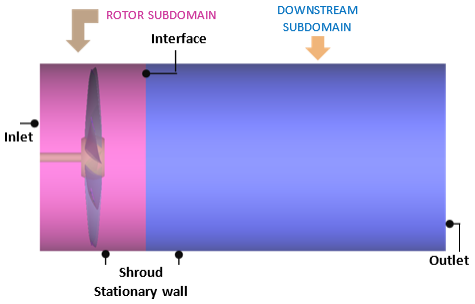


**Fig. 8. Computational domain and the boundary conditions (simulation in steady state).**

*Inlet surface:* The velocity condition is considered, the initial gauge pressure of 0 Pa, turbulence intensity level of 5%, and hydraulic diameter.

*Outlet surface:* The Outflow condition is considered. It is not necessary to establish any characteristic quantity of the flow such as pressure or velocity at the outlet when this condition is used.

*Walls:* The non-slip condition was considered. This condition is used in the solid regions where the fluid circulates. The option of rotational movement ($n$ = *1800 rpm*) in relation to the adjacent cell zone is considered for the hub and the blades. The stationary wall option is considered for the surfaces associated with the shroud and the walls of the inlet and outlet domains.

The mesh on the surfaces of the blades, especially at the tip region and trailing edge, has been carefully refined (with a prismatic layer with 8 levels), so that the values of $y^+$ are close to 1. This way, the first elements are in the region of the viscous sublayer and, consequently, allowing to capture the velocity gradient close to the wall. For the simulation, upwind second-order numerical solution schemes were also used, in order to guarantee the accuracy of the solution.

To couple the inertial and non-inertial domains in the steady-state simulation, the Multiple Reference Frame-MRF was used. With this model the flow in the non-inertial domain is solved using a moving frame of reference and in the inertial domain the equations reduce to stationary forms. At the interfaces of the domains (surfaces that connect them), a local reference system transformation is developed to allow the flow variables of one domain to be used to calculate the flows in the domains of adjacent zones. With MRF the mesh must remain fixed during the solution. This feature is analogous to freezing the motion of the moving part in a specific position and observing the instantaneous flow field with the rotor in that position (Augustyn 2013).

In order to predict the radiated sound in the far field in several receivers, the integral model based on the acoustic analogy of Ffowcs-Williams and Hawkings (FF-WH) was used, considering the source region and the propagation region. For the source region was considered the rotor surfaces. The *k-ω SST URANS* model was used to obtain the sound pressure. The simulation in the unsteady state for sweep blade rotors had as main target to obtain the characteristics of acoustic emission through the implementation of the Fast Fourier Transform.

For the unsteady state simulation, the Sliding Mesh Model-SMM was adopted. With this model, the inertial and the no-inertial domains are also associated with each other through the mesh interfaces (where the variables of the flow field between the surfaces are interpolated in order to guarantee continuity in the variables), and these domains associated through mesh interfaces move relative to each other along the mesh interface.

As for the boundary conditions, the conditions shown in Fig. 9 were imposed in the transient simulations in the Fluent® program:

Therefore, the boundary conditions based on Fig. 8 for unsteady simulation are:

*Inlet surface:* The Mass Flow condition was considered, with turbulence intensity level of 5%, and hydraulic diameter.

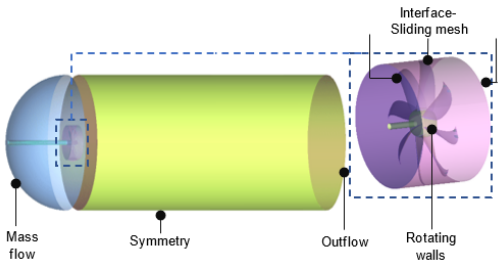


**Fig. 9. Computational domain and boundary conditions (simulation in unsteady state).**

*Outlet surface:* The Outflow condition is considered because there is no value for the static pressure at the outlet.

*Walls:* the non-slip condition is considered with the option of rotational movement in relation to the adjacent cell zone, which must be satisfied on the walls. This condition is used in the solid regions (blades and hub rotors) where the fluid circulates.

*Interfaces:* The interface condition is used by activating the sliding mesh option to couple the rotor domain and the far field domain.

Outer contour of the output domain: Symmetry condition described on Guédel *et al.* (2012).

### 3.4 Timestep Determination

The timestep, is an important parameter, because the results of the acoustic calculation depend on the specified size since the highest possible frequency that the acoustic analysis can generate is based on the size of the time interval of the data from the collected acoustic sources. According to ANSYS INC. (2012) and Kwedikha (2009); the timestep can be determined by the equation:

$$\Delta t_1 = 1/2SF \tag{45}$$

Where SF, is the sampling frequency. A value of *20kHz* was considered for the simulations. Thus, considering the rotation of *1800 rpm*, and *1.5* turns to obtain the frequency spectrum, the $2.5x10^{-5}s$ timestep is considered. Since the Blade Frequency Passing is *240 Hz*.

## 4. RESULTS AND DISCUSSION

This section presents the numerical results of several aerodynamic and aeroacoustics characteristics that were obtained through our numerical simulation for the two axial rotors with sweep blades designed based on the free and non-free vortex conditions.

### 4.1 Global quantities

The curves of total pressure, hydraulic power and efficiency were obtained, as a function of the volumetric flow to analyze the behavior of the projected rotors.

The characteristic curves corresponding to the fan rotor designed with the condition of free vortex -

FV are presented in Fig. 9 a), and the designed rotor with the condition of non-free vortex – NFV is shown in Fig. 9 b).

The best efficiency point (BEP) values of *90.18 %* and *89.98 %* correspond to the flow rates of *2.63 $m^3/s$* and *2.38 $m^3/s$*, for the free vortex (FV) and non- free vortex (NFV) fan rotors respectively (Fig. 9). It is clear that the limit between the region of instability and the region of stability of the rotors, is comprised approximately until the flow of $\dot{V}$ =2.25$m^3/s$ in the case of the FV rotor; and the flow rate of $\dot{V}$ =2.13 $m^3/s$ in the case of the NFV rotor.

The region of instability corresponds to the flows region lower than point A in Fig. 9. The point B indicates the limit between the region of instability and the region of stability of the fan, and is close to the point where the fan stall occurs. As mentioned in Eck (1973), this region must be totally avoided, that is, the axial fan must not be operated with flow rates lower than that referring to point (B).

The points of maximum efficiency of the rotors are in the region of stability, with the FV rotor having a slightly higher operating range. However, it can be seen that the rotor designed with the condition of non-free vortex, NFV, presents a slightly superior behavior for low flow rates, although for larger flows it is inferior to the behavior of the FV rotor.

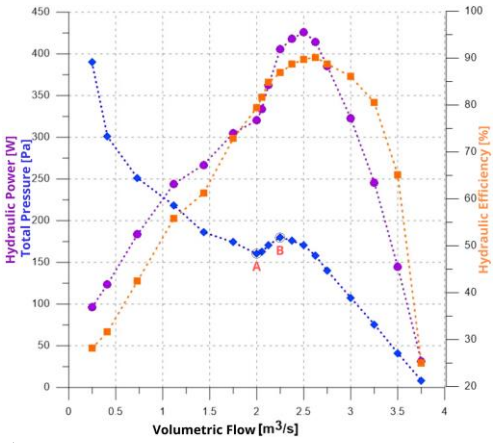


a)

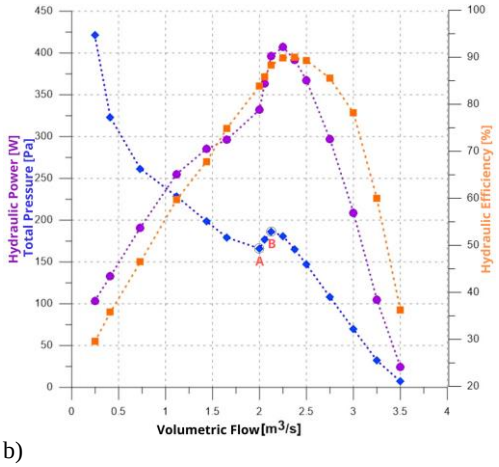


b)

**Fig. 9. Characteristic curves of designed rotors, a) free vortex (b) non-free vortex.**

## 4.2 Local flow fields of the FV and NFV rotors

The static pressure contours of the FV and NFV rotors are represented in Fig. 10, for the best efficiency point. In both rotors, on the suction side of the blade (Fig. 10a), it is observed that the lowest pressures are closer to the leading edge, and the pressure values decrease as they approach the tip of the blade. In the case of the NFV rotor, the low-pressure regions are less extensive when compared to the FV rotor, although the pressure values are lower. The static pressure contours on the pressure side of the rotors (Fig. 10b) indicate that the highest pressures are located closer to the blade tip than to the hub, and in the NFV rotor, these values are lower in these regions.

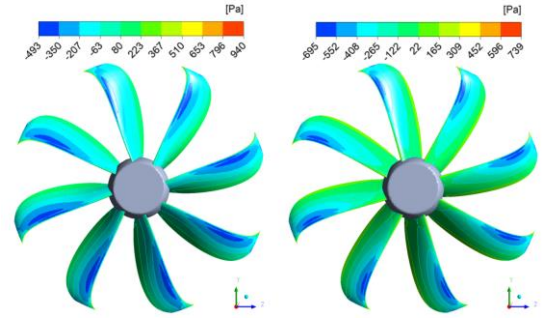


a)

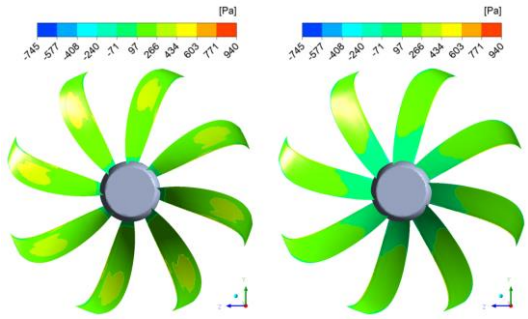


b)

**Fig. 10. Static pressure contours, a) Suction Side; b) Pressure Side.**

In Fig. 11 the contours of the radial component of the velocity in the plane normal to the rotor axis are presented, where it can be observed that this component of the velocity is more accentuated in the region of the hub on the suction side of the blade in both rotors.

The concentration of the radial component of the velocity close to the root of the blades on the suction side of the blades, shown in Fig. 11, can be explained with the behavior of the velocity vectors in the hub region, shown in Fig. 12.

In the case of the FV rotor, the vortex near the trailing edge (Fig. 12a) is larger when compared to the NFV rotor in the same region (Fig. 12b). However, in the case of the NFV rotor, there is also the presence of a vortex on the pressure side at the

root of the blade. Which is consistent with the low pressures in this region identified in Fig. 10.

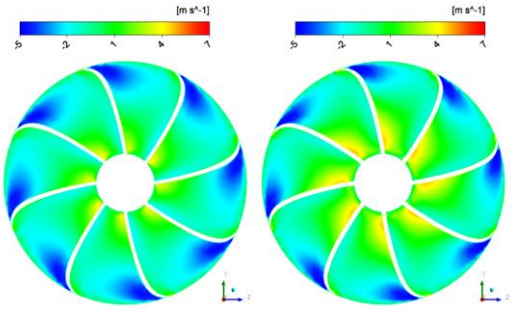

a) b)

**Fig. 11. Contours of radial velocity, a) FV rotor; b) NFV rotor.**

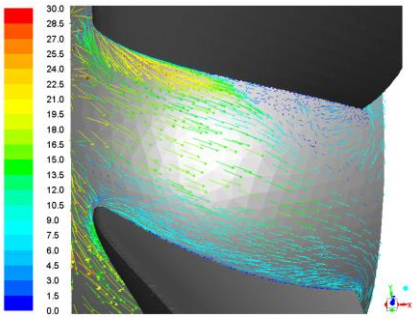

a)

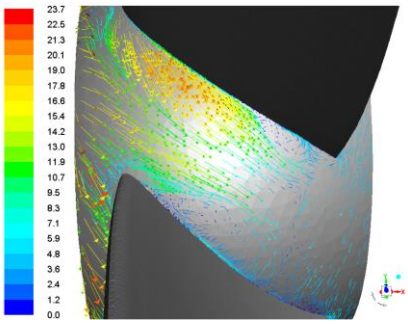

b)

**Fig. 12. Vectors of velocity [m/s] at hub, a) FV rotor; b) NFV rotor.**

The results presented in Fig. 12, are consistent with the typical behavior of fans designed with the Non-Free Vortex condition. In the bibliography (Vad 2012; Masi *et al.* 2016; Corsini and Rispoli 2004) it is reported that rotors designed with this condition have the disadvantage of the presence of the strongest radial component, especially in the hub region. The presence of the radial component of the velocity is associated with the total pressure losses and, consequently, with the fan performance. This was evidenced in the aerodynamic behavior curves presented in Fig. 9, where it can be seen that the NFV rotor has slightly lower total pressure values than the FV rotor in the fan operating region.

Despite this disadvantage, the results show that both designed rotors have a similar operating range in the stable region of the rotor, with similar performance. It is assumed that this is due to the introduction of the circumferential sweep that moderates the radial component of the flow to some extent.

On the other hand, as can be seen in Fig. 13, the tangential velocity values at the tip of the blade show the formation of vortex structures in the region of the blade tip and tip clearance.

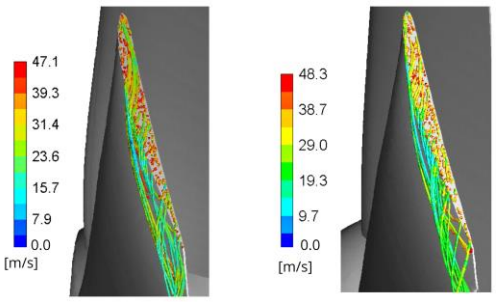


a) b)

**Fig. 13. Tangential component of the velocity at tip blade, a) FV rotor; b) NFV rotor.**

In the case of the NFV rotor, the tangential speed at the tip of the blade is slightly higher when compared to the FV rotor.

### 4.3 Aeroacoustics behavior - Aeroacoustics sources

To identify and to analyze the acoustic sources of the fan rotors, two of the Broadband Noise Source (BNS) models available in the commercially available finite-volume CFD code Fluent® were utilized, which allows the identification of local acoustic sources. These are the Proudman's Formula Model and the Boundary Layer Noise Source Model (ANSYS INC. 2012).

These two models complement each other by giving the dipole and the quadrupole sources in the form of acoustic power (Horváth and Vad 2009) and make it possible to identify the main sources of noise in addition to quantifying their local contribution to the acoustic power generated by the rotors.

In researches conducted by Santos (1995), Khondge *et al.* (2005), Ayar *et al.* (2005), Mohamud and Johnson (2006), Croaker *et al.* (2011), Junger (2019), the Proudman's Formula Model (Proudman 1952) and the Boundary Layer Noise Source Model (Curle 1955) are used and presented as a low-cost computational tool to identify the main noise sources, which represents an attractive option to quickly and inexpensively evaluate the acoustic performance, especially in the design phase, as it allows optimizing the parameters related to the main sources of noise.

Both models are derived from Lighthill's acoustic theory and use the amounts of turbulence calculated from the RANS equations as the mean flow field, turbulent kinetic energy, $k$, and dissipation rate, $\varepsilon$, coupled to acoustic models that consider semi-empirical correlations and the Lighthill acoustic analogy. According to (Dozolme *et al.* 2006), although these models do not require transient

solutions to solve the conservation equations, they are limited to predicting broadband noise characteristics and do not provide accurate information on tonal performance. Therefore, these models are used to identify the main noise generation regions in the form of acoustic power.

Proudman's model (Eq. 46a) is a formula for acoustic power based on the Lighthill acoustic analogy and provides an approximate measure of the local contribution to total acoustic power per unit volume in a given turbulence field. This model applies mainly to noise sources that have their origin in a phenomenon caused by flow separation and vortex formation.

$$SW = \alpha\ \rho_0\left(u^3/l\right)\frac{u^5}{a_0^5}\quad \left[W/m^3\right] \tag{46a}$$

In Proudman's original derivation, α≈13. In terms of $k$ and $\varepsilon$ and using $u^2 = 2k/3$, $\varepsilon = 1.5u^3/l$, the Eq. (46a) can be written as:

$$SW = \alpha_\varepsilon \rho_0 \varepsilon \left(\frac{\sqrt{2\kappa}}{a_0}\right)^5 \quad \left[W/m^3\right] \tag{46b}$$

Where, SW, is the acoustic power; $\alpha_\varepsilon$, is a scaled constant, $\rho_o$, is the ambient density; $\varepsilon$, is the dissipation rate; $\kappa$, is the turbulent kinetic energy; and $a_o$, is the speed of sound. The escaled constant $\alpha_\varepsilon$, is approximately 0.5 for the Proudman's constant (α≈13). Sarkar and Hussaini (1993), based on their DNS (Direct Numerical Simulation) for isotropic turbulence, found results that are in agreement with Proudman's analytical expression, however they recalibrated the constant $\alpha_\varepsilon$ = 0.1, which best fits the DNS data. Thus, in FLUENT it is set to 0.1

The Eq. (46b) makes it possible to determine the sound power due to the unit volume of isotropic turbulence (Khondge *et al.* 2005, Horváth and Vad, 2009).

On the other hand, the Boundary Layer Noise Source Model is based on the Curle's integral, where the radiated acoustic pressure is derived as a function of the fluctuating surface pressure of the blade surface. The model is used to investigate the noise generated by the turbulent flow at the boundary layer. In this one, an approximation is used to determine the local contribution per unit surface area of the body surface, in the total acoustic power, as can be seen in Eq. (47).

$$SW = \int_S I(\vec{y})dS(\vec{y}) \tag{47}$$

where:

$$I(\vec{y}) \equiv \frac{A_c(\vec{y})}{12\rho_0\pi a_0^3}\overline{\left[\frac{\partial p}{\partial t}\right]^2} \tag{48}$$

The $A_c(\vec{y})$ is the correlation area, $S(\vec{y})$ is the integration surface and $I(\vec{y})$ is the sound intensity per unit area of the surface (ANSYS INC. 2012).

The mean-square time-derivative of the surface pressure and the correlation area are further approximated in terms of turbulent quantities like turbulent kinetic energy, dissipation rate, and wall-shear (Khondge *et al.* 2005).

Applying scaling laws, as presented in Croaker *et al.* (2011), it can be shown that:

$$\overline{\left[\frac{\partial p}{\partial t}\right]^2} \propto \frac{1}{T_f^2}|p|^2 \tag{49}$$

Where $T_f$ is the characteristic period of the fluctuation and can be expressed as $T_f \propto L/u^*$, where $L$ is a characteristic length of the surface and $u^*$ is the friction velocity over surface.

The fluctuating pressure due to wall shear stress can be related to the friction velocity as $|p| \propto |\tau_w| \propto \rho u^{*2}$. Therefore, $u^* = \sqrt{\tau_w/\rho}$.

Considering $k_0 \propto u^{*2}$ as the amount of kinetic energy associated with the fluctuating component of the friction velocity, and considering the relation between $k$ and flow shear stress, $\tau$, the $k_0$ is defined as:

$$k_0(y) = \frac{\tau_0(y)\nu_t}{\rho_0 \nu \sqrt{C_\mu}} \tag{50}$$

Where $C_\mu$ is a constant coefficient of the turbulence model, $\tau_0(y)$ is the mean wall shear stress at $y$, $\nu$ is the viscosity of the fluid and $\nu_t$ is the turbulent viscosity. All quantities on the right-hand side of Eq. (50) can be obtained from a steady-state CFD analysis.

A detailed demonstration of the method for estimating the acoustic power due to quadrupole and dipole sources through steady-state CFD data can be found in the work of Croaker *et al.* (2011), where it is shown that the acoustic power expressions corresponding to the dipole sources are obtained from scaling laws of aerodynamic noise previously presented by Lighthill (1952), and extended by Proudman (1952) to obtain the analytical expression of Eq. (46) and by Curle (1955) to develop the boundary layer model for dipole source.

Through the models presented, Proudman's Formula Model (Proudman 1952) and the Boundary Layer Noise Source Model (Curle 1955), the analysis of the sound sources was carried out and the sound power level (*SWL*) for four volumetric flow values of each of the studied rotors (Tables 5 and 6).

The local contribution of the sources caused by the separation of the flow on the rotors surfaces is more evident in the sound power level (*SWL*) range of 60.1 – 90 dB.

In the case of the NFV rotor, for almost all flow rates (except for the low flow point), the sound power level (*SWL*) values in the range of 60.1 - 90 dB, represent a lower percentage when compared to the FV rotor.

**Table 5 Percentage of SWL, FV rotor**

| Q | 0-60 dB | 60.1-90 dB | 90.1-max dB | max |
|---|---|---|---|---|
| $m^3/s$ | % | % | % | dB |
| 0.73 | 19.74 | 78.75 | 1.51 | 112.78 |
| 1.75 | 26.75 | 71.07 | 2.18 | 113.28 |
| 2.62 | 15.35 | 81.23 | 3.42 | 112.84 |
| 3.73 | 6.33 | 88.49 | 5.19 | 118.87 |

**Table 6 Percentage of SWL, NFV rotor**

| Q | 0-60 dB | 60.1-90 dB | 90.1-max dB | max |
|---|---|---|---|---|
| $m^3/s$ | % | % | % | dB |
| 0.73 | 19.22 | 79.23 | 1.55 | 114.22 |
| 1.65 | 28.97 | 68.96 | 2.07 | 112.21 |
| 2.37 | 21.68 | 75.07 | 3.24 | 113.77 |
| 3.73 | 10.41 | 84.51 | 5.08 | 118.46 |

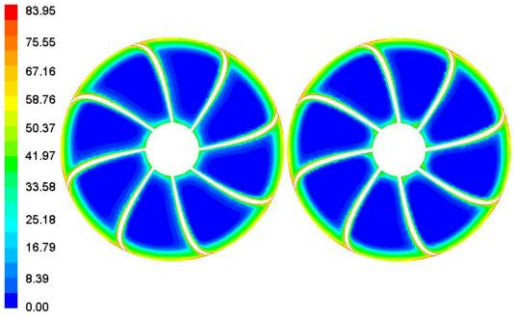


a) b)

**Fig. 14. SWL at plane normal to axis. a) FV rotor, Q=2,63 $m^3/s$; b) NFV rotor, Q=2,38 $m^3/s$.**

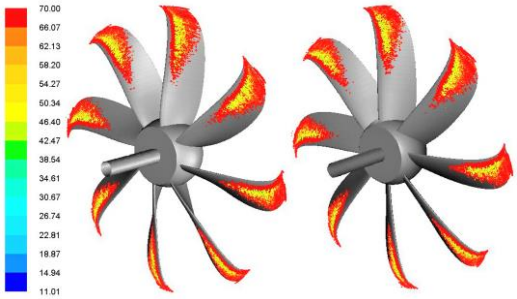


a) b)

**Fig. 15. Isosurfaces colored by Sound Power Level with values up to 70 dB. a) FV rotor; b) NFV rotor.**

Regarding the qualitative results, contours of the local sources of sound were obtained. In Fig. 14, the contours of the sound power level are shown in the plane normal to the axis (x=0). For both rotors, the largest sources are concentrated in the region near the tips of the blades and tip clearance, and in the upper part of the blades suction side. Local sources were also identified, although they are smaller, in the cube region.

In Fig. 15, iso-surfaces colored by Sound Power Level are shown with values up to 70 dB, and it can be seen that the regions that present these values are concentrated in the upper part of the blade. Therefore, the largest sources due to pressure fluctuations are in the region close to the blade tip and tip clearance.

The results in Fig. 15 are related to the low pressure regions identified in the aerodynamic analysis, and in the case of the FV rotor the low pressure region extended from the tip of the blade to approximately half of the blade. And in the case of the NFV rotor, these regions were more concentrated in the region close to the blade tip, being slightly smaller for the latter rotor.

### 4.4 Sound Pressure Level

The acoustic radiation from low-speed fans is divided into the contribution of the tonal noise and the broadband noise. Broadband noise is associated with the turbulent flow field which creates an acoustic radiation distributed throughout the whole frequency spectrum. Tonal noise is generated by the periodic components of the blade load and is characterized by distinct tones in the frequency spectrum (Magne *et al.* 2015).

In order to obtain the sound pressure level for the best efficiency point for FV and NFV rotors, the URANS simulation is carried out. Although the URANS method fails with regard to broadband noise prediction, since the latter requires a numerical method with high precision (Hurault *et al.* 2010), the URANS is a less expensive approach that can help in the prediction of the tonal behavior of a turbomachine in the design phase.

The sound pressure level was obtained considering the ISO 13347-3 (2004) standard. Therefore, receivers 1- 9 were considered according to ISO 13347-3 (Fig. 16 and Table 7). This configuration was used in Mota (2018), where numerical and experimental results were evaluated. In addition, receivers 10, 11 and 12 were positioned at the fan

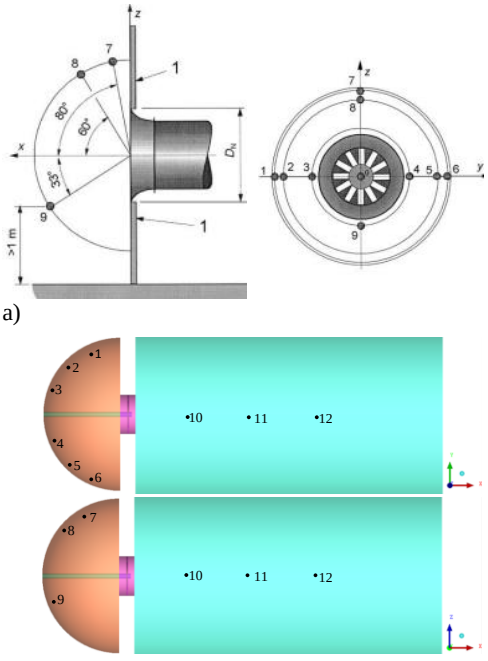


a)

b)

**Fig. 16. Receiver positions, a) according to ISO 13347-3; b) downstream of the fan.**

**Table 7 Position of acoustic measuring points (ISO 13347-3)**

| Reference Position | Angle | x | y | z |
|---|---|---|---|---|
| 1 | 80° | 0.174r | -0.985r | 0 |
| 2 | 60° | 0.500r | -0.866r | 0 |
| 3 | 33° | 0.839r | 0.545r | 0 |
| 4 | 33° | 0.839r | -0.545r | 0 |
| 5 | 60° | 0.500r | 0.866r | 0 |
| 6 | 80° | 0.174r | 0.985r | 0 |
| 7 | 80° | 0.174r | 0 | 0.985r |
| 8 | 60° | 0.500r | 0 | 0.866r |
| 9 | 33° | 0.839r | 0 | -0.545r |

outlet at 1, 2 and 3 meters respectively from the trailing edge. This configuration is adopted by Younsi and Lavedrine (2015) as well and is shown schematically in Fig. 16(b).

The following constants and parameters were considered for the acoustic propagation analysis: the density, *1.225 kg/m*$^3$; the sound velocity *340 m/s* and the reference sound pressure, $2\times10^{-5}$ *Pa*. The rotor surfaces were configured as sources, 1.5 rotations, 2000 timestep of $2.5\times10^{-5}$s, for time of 0.05s. Table 8 convey the results of the sound pressure level, for the different fans considering all receivers.

The mean values of the sound pressure level, obtained through the logarithmic average of the values in Table 8 (receivers 1-9), for the FV and NFV rotors, are 82.2 dB and 80.1 dB, respectively.

According to this analysis, the NFV rotor is 2.2 dB less than the FV rotor. This is in line with the source analysis presented in section 4.3, where the percentage of the sound power level for the BEP was lower for this rotor when compared to the FV rotor.

**Table 8 SPL on receivers according to ISO 13347-3 and positioned downstream of the rotor**

| Sound Pressure Level – SPL [dB] | | |
|---|---|---|
| Receivers | Rotor FV | Rotor NFV |
| 1 | 78.7 | 75.5 |
| 2 | 82.9 | 80.8 |
| 3 | 84.8 | 83.1 |
| 4 | 83.9 | 82.4 |
| 5 | 81.3 | 79.2 |
| 6 | 77.0 | 76.3 |
| 7 | 80.2 | 74.4 |
| 8 | 83.5 | 79.8 |
| 9 | 82.5 | 81.2 |
| 10 | 89.3 | 86.9 |
| 11 | 83.2 | 80.6 |
| 12 | 78.1 | 75.2 |

## 5. CONCLUSION

The analysis of aerodynamic and aeroacoustics characteristics were completed for axial flow fan rotors designed based on the conditions of free and non-free vortex, both with the circumferential sweep effect on the blades.

The geometries were obtained based on the variation of the curve parameters that define the stacking center line for each blade, resulting from the sweep, which in turn is defined by a cubic function that allows better control of the sweep angle at the blade tip.

It is important to highlight that the design point of both rotors is very close to the points of maximum efficiency of the geometries of the analyzed rotors which indicates that the adopted methodology is adequate. The rotors of the analyzed axial fans present a consistent aerodynamic behavior in terms of efficiency and total pressure, since the maximum efficiency values are far from the stall region.

The results of the analysis of the local sources of sound presented, agree with the aerodynamic results, and the largest sources of sound identified are related to regions of low pressure (upper part of the suction side of the blades), the presence of a strong tangential component of the velocity in the region of the blade tip and the detachment of the boundary layer due to the presence of the radial component of velocity (hub region).

Although both rotors present a similar aerodynamic behavior, according to the analysis of local sound sources it was evidenced that the NFV rotor presents a slight decrease in the sound sources.

According Sound Pressure Level analysis, the NFV rotor is 2.2 dB less than the FV rotor. This is in line with the source analysis presented, where the percentage of the sound power level for the BEP was lower for this rotor when compared to the FV rotor.

## ACKNOWLEDGEMENTS

The authors would like to thank to FAPEMIG (Minas Gerais State Research Support Foundation) and Brentech Energia S/A. for their financial support and to LHV (Virtual Hydrodynamics Laboratory) and LabVent (Fans Laboratory of UNIFEI) for their technical support.

## REFERENCES

Aguirre, C., R. Ramirez, W. de Oliveira and F. Avellan (2019). Numerical analysis for detecting head losses in trifurcations of high head in hydropower plants. *Renewable Energy* 131, 197-207.

Albuquerque, R. (2006). Teoria da Asa de Sustentação Aplicada às Máquinas de Fluxo. Mechanical Engineering Institute, Federal University of Itajubá, Minas Gerais, Brazil. (In Portuguese).

*Ansys Inc.* (2012). Ansys Fluent Theory guide. USA.

Asghari, M., M. Mirzabozorg and M. Adami (2019). Aerodynamic optimization of the tangential stacking line of a transonic axial flow compressor rotor using genetic algorithm.

*Journal of the Brazilian Society of Mechanical Sciences and Engineering* 41(37).

Augustyn, O. P. (2013). *Experimental and Numerical Analysis of Axial Flow Fans*. Master Thesis, Faculty of Engineering at Stellenbosch University, South Africa, December.

Ayar, A., R. Ambs, C. Capellmann, B. Schillemeit, M. Matthes. (2005). Prediction of Flow-Induced Noise in Automotive HVAC Systems Using a Combined CFD/CA Approach. *SAE Technical Paper* 2005-01-0509.

Beiler, M. and T. Carolus (1999). Computation and Measurement of the Flow in Axial Flow Fans with Skewed Blades, ASME *Journal of Turbomachinery* 121, 59-66.

Bran, R. and Z. Souza (1969). Máquinas de Fluxo: Bombas, Ventiladores e Turbinas. Livro Técnico S.A. Rio de Janeiro, Brazil. (In Portuguese)."

Camacho, R. and J. Barbosa (2005). The boundary Element Method Applied to Incompressible Viscous Fluid Flow. *Journal of the Brazilian Society of Mechanical Sciences and Engineering* 27(4), pp. 456–462.

Camacho, R. and N. Manzanares Filho (2005). Source Wake Model for Cascades of Axial Flow Turbomachines. *Journal of the Brazilian Society of Mechanical Sciences and Engineering* 27(3), pp. 288–299.

Carolus, T. and M. Beiler (1997). Skewed blades in low pressure fans: a survey of noise reduction mechanisms. American Institute of Aeronautics and Astronautics, 97, 1591.

Castilho, L., R. Ramirez Camacho, E. da Silva (2016). Optimized Design of Linear Cascades For Turbomachinery Applications. *Journal of the Brazilian Society of Mechanical Sciences and Engineering* 38(3), pp. 813–825.

Corsini, A. and F. Rispoli (2004). Using sweep to extend the stall-free operational range in axial fan rotors. Proceedings of the Institution of Mechanical Engineers, Part A: *Journal of Power and Energy* 218: 129.

Cox-Stouffer, S. (1997). *Numerical Simulation of Injection and Mixing in Supersonic Flow*. Ph. D. thesis, Virginia Polytechnic Institute and State University.

Croaker, P., A. Skvortsov and N. Kessissoglou. (2011). A simple approach to estimate flow-induced noise from steady state CFD. *Australian Acoustical Society Conference 2011*, 451-458.

Curle, N. (1955). The Influence of Solid Boundaries upon Aerodynamic Sound, Proceedings of the Royal Society of London Series A, 231, 505-514.

Dachuan, X., W. Haifeng, Q. Xiaoli, Y. Yongsheng, S. Yu and Z. Fang (2019). Application of Arbitrary Vortex Method in Wind Tunnel Axial Fan Design. IOP Conference Series: Materials Science and Engineering, 616, 012006.

Dozolme, A., H. Metwally and T. Marchal (2006). *Electronics Cooling Fan Noise Prediction*. Therminic 2006, Nice, France. TIMA Editions, 75-79.

Eck, B. (1973). *Fans - Design and Operation of Centrifugal, Axial-flow and Cross-flow Fans*. First edition. Pergamon Press, Oxford, New York.

Guédel, A., M. Robitu, N. Descharmes, D. Amor and J. Guillard (2012). Prediction of the blade trailing-edge noise of an axial flow fan. *ASME Turbo Expo 2011*. Paper GT2011-45256, Vancouver, Canada.

Herold, G., F. Zenger and E. Sarradj (2017). Influence of blade skew on axial fan component noise. *International Journal of Aeroacoustics* 16(4–5) 418–430.

Horváth, C. and J. Vad (2009). Broadband noise source model acoustical investigation on unskewed and skewed axial flow fan rotor cascades; Conference on Modelling Fluid Flow (CMFF'09). *The 14th International Conference on Fluid Flow Technologies*. Budapest, Hungary, September 9-12.

Hurault, J., S. Kouidri, F. Bakir and R. Rey (2010). Experimental and numerical study of the sweep effect on three-dimensional flow downstream of axial flow fans. *Journal Flow Measurement and Instrumentation*. 21, 155-165.

*ISO 13347-3* (2004). Industrial fans - Determination of fan sound power levels under standardized laboratory conditions - Part 3: Enveloping surface methods, International Organization for Standardization, Geneva.

Junger, C. (2019). *Computational aeroacoustics for the characterization of noise sources in rotating systems. Doctoral theses.* Vienna University of Technology Faculty of Mechanical and Industrial Engineering.

Khondge, A. D, S. Sovani, S. Kim, S. Guzy and A. Farag (2005). On Predicting Aeroacoustic Performance of Ducts with Broadband Noise Source Models. *SAE Paper*, 2005-01-249.

Krömer, F. and S. Becker (2018). Experimental investigation of the off-design sound emission of low-pressure axial fans with different fan blade skew. *Conference Proceedings of Euronoise*.

Krömer, F., F. Czwielong and S. Becker (2019). Experimental investigation of the sound emission of skewed axial fans with leading-edge serrations. *25th AIAA/CEAS Aeroacoustics Conference*, AIAA 2019-2735.

Kwedikha, A. (2009). *Aerodynamic effects of blade sweep and skew applied to rotors of axial flow turbomachinery*. Ph.D. Thesis. Budapest University of Technology and Economics Faculty of Mechanical Engineering Department of Fluid Mechanics. Budapest.

Lighthill, M. (1952). On sound generated aerodynamically, I. General theory. *Proceedings of the Royal Society A 211*, 564–587.

Magne, S., S. Moreau and A. Berry (2015). Subharmonic tonal noise from backflow vortices radiated by a low-speed ring fan in uniforminlet flow. *Journal of the Acoustical Society of America* 137, 228–237

Masi, M. and A. Lazzaretto (2017). Preliminary investigation on the effect of the modification of the sweep angle at the blade tip of forward swept axial fans. *Proceedings of ASME Turbomachinery Technical Conference and Exposition GT 2017*. June 26-30, Charlotte, NC, USA.

Masi, M., A. Lazzaretto and S. Castegnaro (2018). Effectiveness of Blade Forward Sweep In *A Small Industrial Tube-Axial Fan*. *Conference paper Fan 2018*. Darmstadt, Germany, 18 – 20 April.

Masi, M., S. Castegnaro and A. Lazzaretto (2016). Forward sweep to improve the efficiency of rotor-only tube-axial fans with controlled vortex design Blades. Proceedings of the Institution of Mechanical Engineers, Part A: *Journal of Power and Energy* 230(5), 512-520.

Mohamud, O. M. and P. Johnson. (2006). Broadband noise source models as aeroacoustics tools in designing low NVH HVAC ducts. *SAE Technical Paper* 2006-01-1192.

Mota, P. (2018). *Estudo Aeroacústico Numérico e Experimental de Ventilador Axial.* Master's thesis, Federal University of Itajubá, Minas Gerais, Brazil. (In Portuguese).

Proudman, I. (1952). The generation of noise by isotropic turbulence. *Proceedings of the Royal Society of London Series A*, 214119,132.

Roffi, M., F. Ferreira and A. de Almeida (2017). Comparison of different cooling fan designs for electric motors, *2017 IEEE International Electric Machines and Drives Conference (IEMDC)*, 1-7.

Santos, Roberto M. Moura (1995). *Ruído de helices: Mecanismos de geração e modelagem dos tons discretos*. Master's thesis, Federal University of Rio de Janeiro, Brazil. (In Portuguese).

Sarkar, S. and M. Hussaini. (1993). Computation of the Sound Generated by Isotropic Turbulence, *NASA Contract Report No.* 93-74, NASA Langley Research Center, Hampton VA 24681.

Sarmiento, A. (2013). *Desenvolvimento de uma metodologia para o projeto aerodinâmico de rotores axiais reversíveis de ventiladores de jato de túneis rodoviários*. Master's thesis, Federal University of Itajubá, Minas Gerais, Brazil. (In Portuguese).

Sarmiento, A., R. Ramirez and W. de Oliveira (2020). Performance Analysis of Radial-Inflow Turbine of ORC: New Combined Approach of Preliminary Design and 3D CFD Study. *Journal of Mechanical Science and Technology* 34(6), 2403–2422.

Sarmiento, A., R. Ramirez, W. de Oliveira, V. Gutiérrez, M. Murthi and N. Diaz (2021). Design and off-design performance improvement of a radial-inflow turbine for ORC applications using metamodels and genetic algorithm optimization. *Applied Thermal Engineering* 183(2), 116197.

Sarmiento, A., W. Oliveira and R. Camacho, (2017). Influence of the vortex design method in the performance characteristics of reversible axial rotors. *Journal of the Brazilian Society of Mechanical Sciences and Engineering* 39, 1575–1588.

Suzuki, S., Y. Ugai and K. Komatsu (1985). A study on noise reduction of axial flow fans. In *Proceedings Inter-noise 85* (München, Germany), 371-374.

Vad, J. (2011). *Blade Sweep Applied to Axial Flow Fan Rotors of Controlled Vortex Design*. Doctoral Thesis Hungarian Academy of Sciences. Budapest.

Vad, J. (2012). Incorporation of forward blade sweep in preliminary controlled vortex design of axial flow rotors. Proceedings of the Institution of Mechanical Engineers, Part A: Journal of Power and Energy, 226(4), 462-478.

Vad, J., Halász G. and Benedek T. (2015). Efficiency gain of low-speed axial Flow rotors due to forward sweep. Proceedings of the Institution of Mechanical Engineers, Part A: *Journal Power and Energy* 229(1) 16–23.

Wadia, A., P. Szucs and D. Crall (1998). Inner working of aerodynamic sweep. Journal of Turbomachinery. *ASME paper* 97-GT-401.

Wallis, R. (1983). *Axial Flow Fans and Ducts. First edition*. John Willey & Sons, Inc.

Yahya, S. (1983). *Turbines, Compressors and Fans*. Tata McGraw-Hill Publishing Company Limited.

Yang, L. (2016). Investigation of blade tip of axial rotor with part-span forward skew. *Proceedings of the 2015 International Conference (MME2015- Mechanics and Mechanical Engineering)*, 414 - 420.

Younsi, M. and J. Lavedrine (2015). Unsteady Flow and Acoustic Behaviour of an Axial Fan: Numerical and Experimental Investigations. *Proceedings of 11th European Conference on Turbomachinery Fluid dynamics & Thermodynamics ETC11*, March 23-27, Madrid, Spain.

Zenger, F. and S. Becker (2016). Fluid Mechanical and Acoustic Characterization of Low-Pressure 3Axial Fans with different Blade Skew. *18th International Symposium on the Application of Laser and Imaging Techniques to Fluid Mechanic. Portugal*. July 4 – 7.